Molecular Neurobiology (2019) 56:4838–4854
https://doi.org/10.1007/s12035-018-1412-2

A Novel *Mecp2*^{Y120D} Knock-in Model Displays Similar Behavioral Traits But Distinct Molecular Features Compared to the *Mecp2*-Null Mouse Implying Precision Medicine for the Treatment of Rett Syndrome

Anna Gandaglia[1] · Elena Brivio[1,2] · Sara Carli[1] · Michela Palmieri[1] · Francesco Bedogni[1] · Gilda Stefanelli[1,3] · Anna Bergo[4] · Barbara Leva[4] · Chiara Cattaneo[1,5] · Lara Pizzamiglio[6] · Marco Cicerone[1] · Veronica Bianchi[1] · Charlotte Kilstrup-Nielsen[4] · Ilda D'Annessa[7] · Daniele Di Marino[8] · Patrizia D'Adamo[1] · Flavia Antonucci[6] · Angelisa Frasca[6] · Nicoletta Landsberger[1,6]

Received: 15 May 2018 / Accepted: 24 October 2018 / Published online: 6 November 2018

Abstract

MeCP2 is a fundamental protein associated with several neurological disorders, including Rett syndrome. It is considered a multifunctional factor with a prominent role in regulating chromatin structure; however, a full comprehension of the consequences of its deficiency is still lacking. Here, we characterize a novel mouse model of *Mecp2* bearing the human mutation Y120D, which is localized in the methyl-binding domain. As most models of *Mecp2*, the *Mecp2*^{Y120D} mouse develops a severe Rett-like phenotype. This mutation alters the interaction of the protein with chromatin, but surprisingly, it also impairs its association with corepressors independently on the involved interacting domains. These features, which become overt mainly in the mature brain, cause a more accessible and transcriptionally active chromatin structure; conversely, in the *Mecp2*-null brain, we find a less accessible and transcriptionally inactive chromatin. By demonstrating that different *MECP2* mutations can produce concordant neurological phenotypes but discordant molecular features, we highlight the importance of considering personalized approaches for the treatment of Rett syndrome.

Keywords MeCP2 · Rett syndrome · Mouse models · Chromatin accessibility · Chromatin binding

Introduction

Mutations in the X-linked *MECP2* (methyl-CpG-binding protein 2) gene cause a large spectrum of neurological disorders. Among these, Rett syndrome (RTT, OMIM #312750) was the first identified and remains the most thoroughly characterized *MECP2*-related disorder [1, 2]. RTT is a pediatric neurodevelopmental disease that typically affects girls, as males fail to survive beyond the first few years of life. Hallmark of typical RTT is the regression of language and hand use after a period of apparently normal development that usually lasts 6–18 months. During and after this regression

Electronic supplementary material The online version of this article (https://doi.org/10.1007/s12035-018-1412-2) contains supplementary material, which is available to authorized users.

✉ Nicoletta Landsberger
nicoletta.landsberger@unimi.it

[1] Neuroscience Division, IRCCS San Raffaele Scientific Institute, 20132 Milan, Italy

[2] Department of Stress Neurobiology and Neurogenetics, Max Planck Institute of Psychiatry, International Max Planck Research School for Translational Psychiatry, 80804 Munich, Germany

[3] Department of Psychology, University of Toronto Mississauga, Mississauga, Ontario L5L 1C6, Canada

[4] Department of Biotechnology and Life Sciences, University of Insubria, 21052 Busto Arsizio, VA, Italy

[5] Department of Molecular Oncology and Immunology, the Netherlands Cancer Institute, 1066 CX Amsterdam, The Netherlands

[6] Department of Medical Biotechnology and Translational Medicine, University of Milan, 20100 Milan, Italy

[7] Istituto di Chimica del Riconoscimento Molecolare, CNR (ICRM-CNR), 20131 Milan, Italy

[8] Department of Informatics, Institute of Computational Science, Università della Svizzera Italiana, 6900 Lugano, Switzerland

phase, patients develop a host of symptoms that typically include intellectual disability, respiratory abnormalities, hand stereotypies, ataxia, absence of speech, autonomic dysfunctions, and epilepsy.

Although a comprehensive understanding of all its functions is still missing, MeCP2 is commonly defined as a ubiquitously expressed multifunctional protein mainly working as a transcriptional repressor. MeCP2, in fact, consists of two fundamental domains: a methyl-CpG binding domain (MBD) mediating its preferential binding to methylated DNA and a transcriptional repression domain (TRD) inhibiting gene expression through different mechanisms, including the recruitment of chromatin remodeling complexes to methylated DNA [3–6]. Moreover, in mature neurons, where MeCP2 is very abundant, the protein acts as an alternative linker histone, organizing a specialized chromatin structure that dampens transcriptional noise [7].

Even if most cases of RTT are caused by missense and nonsense mutations in *MECP2*, the first and so far most studied *Mecp2* model has been the full knockout mouse, generated and described in refs. [8, 9]. However, to mimic RTT more closely, few more animal models carrying human pathogenic mutations have been generated [10, 11].

Typically, *Mecp2* mouse models recapitulate many RTT features. In particular, the hemizygous males appear grossly normal in the perinatal period, but later, they develop a progressive neurological phenotype whose onset and severity depend on the specific genetic mutation. These mice manifest locomotor deficits, hind limb clasping, hypotonia, reduced spontaneous movements, tremors, breathing defects, and seizures [10]. While the complete absence of *Mecp2* results in a premature death, generally occurring between 56 and 80 days of life [8, 9], the lifespan of knock-in mice can vary from 95 to 110 days to more than 300, according to the severity of the mutation [12].

Interestingly, several lines of evidence suggest that in null animals, Mecp2 functions might be replaced by one or more other proteins, which therefore mask the consequences of its lack [7]. This suggests the importance of producing knock-in models that by ensuring the presence of the mutated protein, might provide better insights into MeCP2 functions [5, 10, 12–14]. For example, the $Mecp2^{R306C}$ model was pivotal in revealing the recruitment of the NCoR/SMRT corepressor on DNA as a core MeCP2 function [5]. Similarly, $Mecp2^{T158M}$ and $Mecp2^{R133C}$ mutations in mice were instrumental to determine the role of the MBD on protein stability and chromatin binding [12].

We have recently highlighted the relevance of Tyr-120 (Y120) residue for MeCP2 structure and function [15]. Its involvement in RTT was suggested by the identification of a patient carrying the pathogenic substitution of Y120 with aspartic acid (Y120D) [16]. The residue Y120 is located in the MBD of MeCP2, and it is highly conserved in mammals. In accordance with its location, we proved that the substitution of residue Y120 with a D impairs the ability of the MBD to interact with DNA [15]. Accordingly, previous studies demonstrated that an exogenously expressed MeCP2-Y120D derivative features a decreased affinity for heterochromatin [17, 18].

Based on these evidences and driven by the idea that specific mutations produce molecular consequences that might differ from the lack of *Mecp2*, we generated a novel mouse model carrying the human pathogenic mutation Y120D. We demonstrate that $Mecp2^{Y120D}$ mice show a harsh behavioral phenotype that is only slightly less severe than *Mecp2*-null mice. At the molecular level, the Y120D mutation impairs the ability of Mecp2 to acquire a tight binding to chromatin mainly in mature neurons and to recruit corepressors on heterochromatin. As a consequence, compared to the *Mecp2*-null model, the Y120D adult brain is characterized by a globally more open chromatin structure. Our data suggest that, in spite of overlapping RTT-like symptoms, different mouse models of *Mecp2* might display largely different molecular phenotypes, a novel perspective for the field of Mecp2 studies. Furthermore, while our results reinforce the idea that Mecp2 functions change with brain maturation [7, 19], they challenge the general perception of the impact of Mecp2 mutations on neuronal chromatin architecture.

Materials and Methods

Plasmids

Human eGFP-MeCP2-WT and its mutant derivatives eGFP-MeCP2-Y120D and -Y120F were obtained and described in [20]. The TBL1-mCherry construct [5] was kindly provided by Dr. Adrian Bird (Wellcome Trust Centre for Cell Biology, University of Edinburgh, UK).

Animal Husbandry

Both mouse lines were housed in the animal facility of the San Raffaele Scientific Institute of Milan. Generation of the knock-in (KI) mouse line is described in Supplementary Materials and Fig. S1. $Mecp2^{Y120D/y}$ males, heterozygous females, and wild-type (WT) controls were obtained by crossing heterozygous females with WT males of either C57BL/6J or CD1 background purchased from Charles River. Genotyping was performed through PCR on genomic DNA purified from tail biopsies, using the following primers: common forward 5′–CAGGGCCTCAGAGACAAGC–3′; common reverse 5′–GCAGATCGGCCAGACTTCC–3′; reverse for the KI allele 5′–GGGTTAATTGATATCCAATTGGGATCC–3′. A 300-bp fragment is common for WT and knock-in animals, while a 550-bp fragment is specific for the mutated one. When needed

(e.g., embryos for primary cell cultures or small pups), the animal sex was determined by using primers recognizing *Jarid1* (forward 5′–CCAGGATCTGACGACTTTCTACC–3′, reverse 5′–TTCTCCGCAATGGGTCTGATT–3′), which produce a PCR fragment only in males.

Mating and genotyping of the CD1 *Mecp2*^{Bird} mouse line are described in [21].

All procedures were performed in accordance with the European Community Council Directive 2010/63/UE for care and use of experimental animals; all the protocols were approved by the Italian Minister for Scientific Research and by the San Raffaele Scientific Institutional Animal Care and Use Committee in accordance with the Italian law.

Phenotypic Evaluation

C57BL/6J or CD1 knock-in mice and WT littermates were weekly tested for the presence or absence of RTT-like symptoms with a previously described scoring system [22]. During each session, mice were weighed and scored for their general condition, mobility, hind limb clasping, and (only for CD1) tremor. Of note, the intermediate values of 0.5 and 1.5 were added to the canonical scores between 0 and 2 to provide a more detailed description of the phenotypic variability (for details see Supplementary Materials). All animals scoring 2 for general condition or tremor or rapidly losing weight were euthanized for ethical reasons. At the experimental endpoint, animals were euthanized through cervical dislocation after deep anesthesia with Avertin (Sigma-Aldrich, St Louis, MO, USA). At the time of death, brains were quickly removed and weighed, and cortices dissected on ice. Day of euthanasia was considered as day of death without distinguishing it from natural death.

Behavioral Assessment

Animals were maintained on an inverted 12-h light/darkness cycle at 22–24 °C.

Rotarod Rotarod apparatus is composed by a horizontal rotating rod (diameter 3 cm) on which mice, separated by large disks, have to keep their balance. The test was carried out in 2 days. Each day, five trials of 5 min, separated by intervals of 30 min, were presented to the mice. On day 1, mice were placed on the apparatus with the rod rotating at 4 rpm (rotations/min) for 1 min, and then, the rotation speed was increased every 30 s by 4 rpm. On day 2, mice were tested at a constant rotation speed corresponding to the average of the maximum speeds reached from all mice during day 1. A trial ended when the mouse fell down or after 5 min. The latency to fall down from the rod was taken as the dependent variable for every trial and was normalized for the mouse weight.

Grip Grip test was performed with a horizontal metal bar (grip) strength dynamometer that mice grasp with the forelimb while suspended by their tail. Animals were gently pulled backward until they released the grip. The dependent variable was the maximal value obtained on a total of six trials.

Catwalk Gait analysis was performed by using CatWalk XT System (Noldus Information Technology, Wageningen, the Netherlands, http://www.noldus.com). Mice were allowed to freely ambulate along an illuminated glass plate within a confined corridor (50 × 8 cm) in a darkened room; footprints were recorded with a high-speed camera and subsequently analyzed with CatWalk XT 10.0 software (Noldus). Three trials/animal were analyzed and averaged to obtain stride length and base of support for front and hind right and left paws.

Spontaneous Alternation The test was performed in a dim illuminated room and mice were habituated to the environment for 1 h before the test. The apparatus consisted in a cross maze with a central hub where the mouse was released and left free to explore for 10 min. Number and sequence of entries in each arm were recorded throughout the test. An alternation was considered correct when no more than one repetition over five entries was made.

Trace Fear Conditioning Auditory trace and delay fear conditioning were performed by placing the mice in an opaque conditioning chamber (L × W × H 25 × 17 × 23 cm; UgoBasile Instrument [Gemonio, Italy]) with a grid floor through which scrambled foot shocks could be delivered as unconditioned stimuli (US; 0.26-mA average intensity). The chamber was placed into a dimly lit (< 5 lx) sound attenuating box (background noise level 55 dB), and a speaker on top of the chamber allowed to deliver sounds as conditioning stimuli (CS; 2000 Hz).

All mice were pre-exposed to the test chamber for 10 min on the day before conditioning. Conditioning consisted in 1 min of baseline period (no stimulus) followed by five trials separated by 1 min of inter-trial intervals (ITI). In the trace fear conditioning, every trial is composed by the presentation of the CS (15 s) followed, 15 s later (trace), by the presentation of the shock for 2 s. The freezing behavior was measured during the presentation of the CS. Twenty-four hours after fear conditioning, mice were placed again in the conditioning box, measuring their freezing behavior in the context test and tone test. Context testing consisted of 2 min without CS ("contextual freezing"); tone testing consisted of 1 min without CS followed by 1 min with the CS turned on in a new environment.

Data Analysis During dark and light, emergence, and novelty tests, animals were video-tracked using the EthoVision 2.3

system (Noldus Information Technology) with an image frequency of 4.2/s. Raw data were transferred to Wintrack 2.4 for off-line analyses (http://www.dpwolfer.ch/wintrack). During fear conditioning test, animals were continuously video-tracked using the ANY-maze system (Anymaze, Stoelting Co., Wood Dale, IL, USA, www.anymaze.com). The frequency of freezing (absence of movements except respiration) was continuously recorded. Statistical computations were done using StatView 5.0 (SAS Institute, Cary, NC, USA). Analysis of variance (ANOVA), alpha value 5%, with factorial measures, was used to test the statistical significance between genotype effect.

Primary Cell Cultures

WT and *Mecp2*$^{Y120D/y}$ neurons were prepared from E15.5 or E17.5 cortices isolated from pregnant heterozygous females. Dissected tissues were washed in HBSS (Life-Technologies, Carlsbad, CA, USA), digested with 0.25% trypsin-EDTA (Invitrogen, Carlsbad, CA, USA) and mechanically dissociated in dissecting medium (DMEM [Sigma-Aldrich], 10% horse serum [Euroclone, Pero, MI, Italy], 1% glutamine [Sigma-Aldrich]). Cells were resuspended in neuronal culture medium (Neurobasal [Life Technologies], 2% B-27 [Life Technologies], 1% glutamine) and plated on 0.1 mg/ml poly-L-lysine (Sigma-Aldrich) both on 6-multiwell plates at a density of 200,000 cells/well and on 24-multiwell plates (containing glass coverslips) at a density of 20,000 cells/well.

Mecp2-null mouse embryonic fibroblasts (MEF) were prepared from *Mecp2*$^{-/y}$ CD1 E14.5 embryos as previously described [20]. For DNA transfection, MEFs were plated on 12-multiwell plates on glass coverslips and transfected with lipofectamine 3000 (Invitrogen) as instructed by the manufacturer. Cells were analyzed 24 h after transfection.

Western Blot

Whole brains and cortices harvested from *Mecp2*$^{+/y}$ and *Mecp2*$^{Y120D/y}$ mice were mechanically homogenized with a Potter-ELV glass grinder in lysis buffer (50 mM Tris-HCl pH 7.4, 500 mM NaCl, 1% Triton X-100, 2 mM EDTA, 1 mM DTT, 1× PhosSTOP [Roche, Basel, Switzerland], 1× complete EDTA-free protease inhibitor cocktail [Roche]). Lysates were incubated 30 min on ice and sonicated (amplitude = 100%, three pulses for a total of 13 min). After centrifugation at 13,000 rpm at 4 °C for 15 min, supernatant was collected. Neurons from 6-multiwell plates were directly lysed in Laemmli buffer 6× and sonicated (*A* = 100%, for 13 min). Proteins were electrophoretically separated on SDS-polyacrylamide gel and blotted on a nitrocellulose membrane using the Trans-Blot Turbo Transfer System from Bio-Rad (Hercules, CA, USA). Membranes were incubated 30 min in blocking solution (Tris-buffered saline containing 5% nonfat milk and 0.1% Tween-20, pH 7.4) and then incubated with the primary antibody diluted in blocking solution overnight at 4 °C. The following primary antibodies were used: rabbit α-MeCP2 (1:1000; Sigma-Aldrich), mouse α-TuJ1 (1:10000; Sigma-Aldrich), rabbit α-rpS6 (5G10, 1:1000; Cell Signaling Technology, Danvers, MA, USA), rabbit α-P-rpS6 (Ser240/244, 1:1000; Cell Signaling Technology), rabbit α-P-S164 (1:1000; Covance, Princeton, NJ, USA), and rabbit α-H1 (1:1000; GeneTex, Irvine, CA, USA). Secondary antibodies were either fluorescent (1:2000 AlexaFluor 488; Life Technologies) or HRP-conjugated (1:10000; Cell Signaling Technology). Signals were visualized and acquired using the fluorescence laser scanner Typhoon FLA 9000 or using the chemiluminescence detection systems UVITEC ChemiDoc (Alliance 9.7, UVITEC Cambridge) or ChemiDoc Touch Imaging System (Bio-Rad). Quantitative analyses were performed using either ImageJ software or ImageLab software from Bio-Rad.

Immunofluorescence and Histology

Cells cultured on glass coverslips were washed with PBS and fixed in 4% paraformaldehyde (PFA) for 20 min at room temperature (RT). Neurons were then permeabilized in 0.1% Tween-20 for 10 min at RT and blocked for 1 h at RT (blocking solution 10% horse serum [Euroclone], 0.1% Triton X-100 in PBS), followed by an overnight incubation at 4 °C with the rabbit α-MeCP2 primary antibody (1:100; Sigma-Aldrich) diluted in blocking solution. Cells were incubated with fluorescent secondary antibody (AlexaFluor 488 α-rabbit, 1:500 in blocking solution) for 1 h at RT. Finally, DNA was counterstained with DAPI (1:1000 in PBS; Invitrogen) for 10 min at RT, and coverslips were mounted with Prolong Gold reagent (Invitrogen).

Transfected MEFs were stained with DAPI (10 min at RT) after fixation. Images were acquired using Nikon microscope, objectives, and software.

Mice were transcardially perfused with 4% PFA. Brains were harvested, cryoprotected in sucrose 30%, and embedded in Tissue-Tek O.C.T. Compound (Sakura Finetek, Alphen aan den Rijn, The Netherlands) and cut in 12-μm sections. Sections were washed thoroughly in PBS, antigen retrieved in 10 mM sodium citrate, washed in 0.01% Tween-20, and incubated in 0.1 M glycine. Tissues were blocked in blocking solution and incubated with antibodies as above (primary antibody: α-ATRX H-300 1:100, Santa Cruz Biotechnology, Dallas, TX, USA; secondary antibody: AlexaFluor 568 α-rabbit, 1:500). After counterstaining with DAPI, sections were mounted with Fluoromount-G (eBioscience, San Diego, CA, USA). Images were acquired using a Leica SP5 confocal microscope.

RNA Pol II-S5P staining was performed on nuclei isolated from *Mecp2*$^{+/y}$, *Mecp2*$^{Y120D/y}$, and *Mecp2*$^{-/y}$ cortices at P40

(as described beneath in the chromatin accessibility assay section). In detail, nuclei were permeabilized in PBST (0.01% Triton X-100 in PBS), fixed in 4% PFA, and spotted on slides prior staining. Nuclei were then blocked for 1 h at room temperature (RT) and incubated overnight at 4 °C with α-RNA Polymerase II-S5P (1:100, Abcam, ab5131). After washing in PBS, nuclei were incubated with AlexaFluor 488 α-rabbit (1:500; Life Technologies) for 2 h at RT, counterstained with DAPI for 10 min at RT, and finally mounted with Fluoromount-G (eBioscience). All images were acquired using a Leica SP5 confocal microscope, and the RNA Polymerase II-SP5 activity was evaluated by measuring the intensity of the nuclear α-RNA Polymerase II-S5P signal using ImageJ Software.

Salt Extraction Assay

Mecp2 chromatin affinity was assessed in brain tissues by performing salt extraction assays as described in refs. [3, 19].

RNA Purification, cDNA Synthesis, and qPCR

Total RNA was extracted from *Mecp2*$^{+/y}$ and *Mecp2*$^{Y120D/y}$ cortices using the RNeasy Mini Kit (QIAGEN, Hilden, Germany) following the manufacturer's instructions. RNA quality was assessed on 1% agarose gel. Total RNA was retro-transcribed using the RT2 First Strand Kit (QIAGEN). qPCRs were performed using SYBR Select Master Mix (Applied Biosystems, Foster City, CA, USA) and the following primers:

Mecp2

- Forward: 5′ AAACCACCTAAGAAGCCCAAATC 3′
- Reverse: 5′ TTGACAACAAGTTTCCCAGGG 3′

18S

- Forward: 5′ GTAACCCGTTGAACCCCATT 3′
- Reverse: 5′ CCATCCAATCGGTAGTAGCG 3′

All samples were evaluated in triplicate and *18S* was used as normalizer.

Calcium Imaging in Cultured Neurons

Cortical neurons at days in vitro (DIV) 4 or 13 were loaded with 5 mM of the ratiometric Ca^{2+} dye Fura-2 pentacetoxymethylester (Sigma-Aldrich) dissolved directly in neuronal medium solution for 35–40 min at 37 °C, washed, and transferred to the recording chamber of an inverted microscope (Axiovert 100; Zeiss, Oberkochen, Germany) equipped with a calcium imaging unit [23]. Fluorescence images were obtained by alternatively illuminating cells at 345 nm and 380 nm wavelength, and images (345 nm or 380 nm) were acquired at 1-Hz frequency. After baseline acquisition, neurons were stimulated with 100 μM NMDA (Tocris) followed by 50 mM KCl. Temporal Ca^{2+} intensity profiles (expressed as ΔF340/380 fluorescence ratio) were calculated in discrete areas of interest from image sequences. Changes over baseline in the ΔF340/380 fluorescence ratio higher than "100" were considered "calcium peak." To induce an appropriate NMDA stimulation, experiments were conducted in Mg^{2+}-free Krebs-Ringer solution (KRH, in order to remove the Mg^{2+} block from the receptor) with tetrodotoxin 1 mM (TTX), while the KCl-induced depolarization has been reached by using normal KRH with 1 μM TTX. Calcium transients were analyzed in about 150–200 cells per experimental group (as specified in legends). Nine glasses per group (one field/glass) were analyzed at each developmental point.

Chromatin Accessibility Assay

To maintain nuclei intact, *Mecp2*$^{+/y}$, *Mecp2*$^{Y120D/y}$, and *Mecp2*$^{-/y}$ brains were mechanically homogenized on ice with Potter-ELV glass grinder in buffer A (0.25 M sucrose, 60 mM KCl, 15 mM NaCl, 10 mM MES pH 6.5, 5 mM $MgCl_2$, 1 mM $CaCl_2$, 0.5% Triton X-100, 1× PhosSTOP [Roche], 1× complete EDTA-free protease inhibitor cocktail [Roche]). Samples were incubated on ice for 10 min and centrifuged at 7000 rpm at 4 °C for 10 min. Supernatants were discarded and nuclei were washed with buffer A. Nuclear pellets were resuspended in the digestion buffer B (50 mM NaCl, 10-mM pipes pH 6.8, 5 mM $MgCl_2$, 1 mM $CaCl_2$, 1× PhosSTOP, 1× complete EDTA-free protease inhibitor cocktail). Fifty microliters of each sample were collected, supplemented with 3 μl of 0.5 M EDTA and conserved as undigested fractions. The remaining volume was pre-warmed at 37 °C and supplemented with 2.5 U of MNase (Worthington Biochemical Corporation, Lakewood, NJ, USA) per 10 million of nuclei. Digested fractions were collected at the indicated time points. MNase digestion was stopped by adding 3 μl of 0.5 M EDTA to each fraction. DNA was phenol/chloroform extracted and quantified. For each fraction, 10 μg of DNA was loaded on a 2% EtBr agarose gel, which was run for approximately 5 h. For each time point, ImageJ was used to obtain a densitometry plot and the amount of mononuclesomal DNA normalized on total DNA was plotted to highlight differences in the digestion rate between experimental groups.

DAPI Staining of MNase-Treated Nuclei

Fresh isolated nuclei were obtained as above. Samples were resuspended in 300 μl of buffer B and 2.5 U/50 μl of MNase were added. Reactions were performed at 37 °C and stopped

at 0, 5, and 10 min by adding 3 μl of 0.5 M EDTA. Nuclei were then fixed in 4% PFA for 5 min, spotted on a glass coverslip and stained with DAPI for 10 min at RT. Nuclei were mounted with Fluoromount-G and imaged using a Leica SP5 confocal microscope. DAPI intensity and heterochromatin area were calculated by using ImageJ software.

5-hmC DNA ELISA Assay

Brain cortices were harvested from *Mecp2*$^{+/y}$, *Mecp2*$^{Y120D/y}$, and *Mecp2*$^{-/y}$ P40 mice. Genomic DNA was extracted from ≤ 25 mg of frozen brain cortices by using the Quick-DNA™ Miniprep Plus Kit (Zymo Research, Irvine, CA, USA) according to the manufacturer's instructions, with the exception that tissues were digested overnight with proteinase K. The percentage of 5-hmC in 100 ng of single-stranded DNA was quantified with the Quest 5-hmC™ DNA ELISA Kit (Zymo Research), following the manufacturer's instructions. HRP color was allowed to develop for 30 min before reading plates at 415 nm with the Microplate Reader Model 680 (Bio-Rad).

Results

Mecp2^{Y120D} Knock-in Mice Manifest a Severe RTT-Like Phenotype and Short Lifespan

The mouse line carrying the human Y120D mutation was generated on a C57BL/6J background (*Mecp2*^{Y120D} mice; Fig. 1a; see Supplementary Materials and Fig. S1 for a detailed description of the procedures). Sequencing of hemizygous mutant mice, screened by PCR, proved the presence of the expected mutation (Fig. 1b).

While the colony was maintained on a C57BL/6J background, the mutant allele was also transferred on a CD1 (ICR) genetic background; the advantages of the CD1 background in Mecp2 studies are described in ref. [21]. Colonies were maintained by crossing heterozygous females to wild-type (WT) males, since hemizygous males were unable to induce pregnancy. To be noticed, the generated mutation does not affect *Mecp2* mRNA levels (Fig. 1c).

The severity of the Mecp2-Y120D mutation was evaluated using a well-established panel of parameters which include lifespan and phenotypic score [22]. As depicted in Fig. 1d, hemizygous *Mecp2*^{Y120D} males died prematurely (average lifespan of 97 and 121 days in the C57BL/6J and CD1 background, respectively). After weaning, mutated males became progressively symptomatic, as indicated by the increased phenotypic score (Fig. 1e; Supplementary Materials and Fig. S2). On the other hand, heterozygous CD1 *Mecp2*^{Y120D} females started showing typical RTT-like features only at 9 weeks of age (Fig. 1f; Supplementary Materials and Fig. S2), and they did not manifest any apparent reduced longevity in the first year of life. C57BL/6J heterozygous females were not analyzed in this study because in a time frame of over 2 years, we did not succeed in generating a sufficient number of animals. In both sexes, similarly to null animals [21], tremor was the first symptom to appear along with worsening of the general conditions, while hind limb clasping and altered mobility appeared later and were characterized by higher variability (Supplementary Materials and Fig. S2). Body weight of *Mecp2* animal models generally depends on mutation, sex, and genetic background [21]; indeed, C57BL/6J *Mecp2*-null mice are notoriously underweight compared to WT, while the corresponding females are generally heavier. Compared to WT, *Mecp2*-null male animals on a CD1 background show no difference in body weight both at early and late postnatal time points. However, CD1 heterozygous females have a strong tendency towards obesity [21]. Our data show that while C57BL/6J *Mecp2*^{Y120D} males were always lighter than WT littermates, CD1 mutated males showed a tendency to be lighter soon after birth, while becoming generally overweight in adulthood (Fig. 1g). Conversely, the body weight of CD1 *Mecp2*^{Y120D} heterozygous females was indistinguishable from WT littermates at early postnatal days, but it progressively increased with aging, leading to obesity (Fig. 1h).

An early diagnostic criterion for Rett syndrome is deceleration of head growth, which often leads to microcephaly in infancy. Similarly, most of the *Mecp2* animals generated so far (with the exception of the *Mecp2*^{308X} mice [24]) are characterized by decreased brain size and weight. We weighed brains of pre- (P18) and symptomatic (P40 and P>130) CD1 *Mecp2*^{Y120D} males. Compared to WT, CD1 mutant brains exhibited an overall weight reduction of 12%, 13.5%, and 17.5% at P18, P40, and P>130, respectively; brains from symptomatic C57BL/6J *Mecp2*^{Y120D} males ($P > 80$) had a 15.7% of weight reduction compared to WT brains (Fig. 1i).

The presence of RTT-like phenotypes was also analyzed through a battery of behavioral tests on CD1 *Mecp2*^{Y120D} male mice and littermate controls. Results are summarized in Fig. 2 and Table S1. Rotarod (Fig. 2a), CatWalk (Fig. 2b, c), and grip (Fig. 2d) tests highlighted significant deficits in motor coordination, gait, and anterior paws strength in juvenile (P30) and/or adult (P60) *Mecp2*^{Y120D} mice.

We next examined learning ability of P30 and P60 *Mecp2*^{Y120D} mice by performing the spontaneous alternation test. Working memory impairment was evident at P30, when knock-in mice showed more than 30% reduction of correct responses with respect to controls, with no difference in the total number of visits (Fig. 2e). P60 data have been omitted since the considerable decrease in spontaneous locomotor activity confounded the interpretation of results. We also found a deficit in associative memory through contextual and cued fear-conditioning tests (Fig. 2f). Juvenile and adult knock-in mice showed significant reduced freezing during the cue exposure 24 h after training, suggesting a specific impairment in

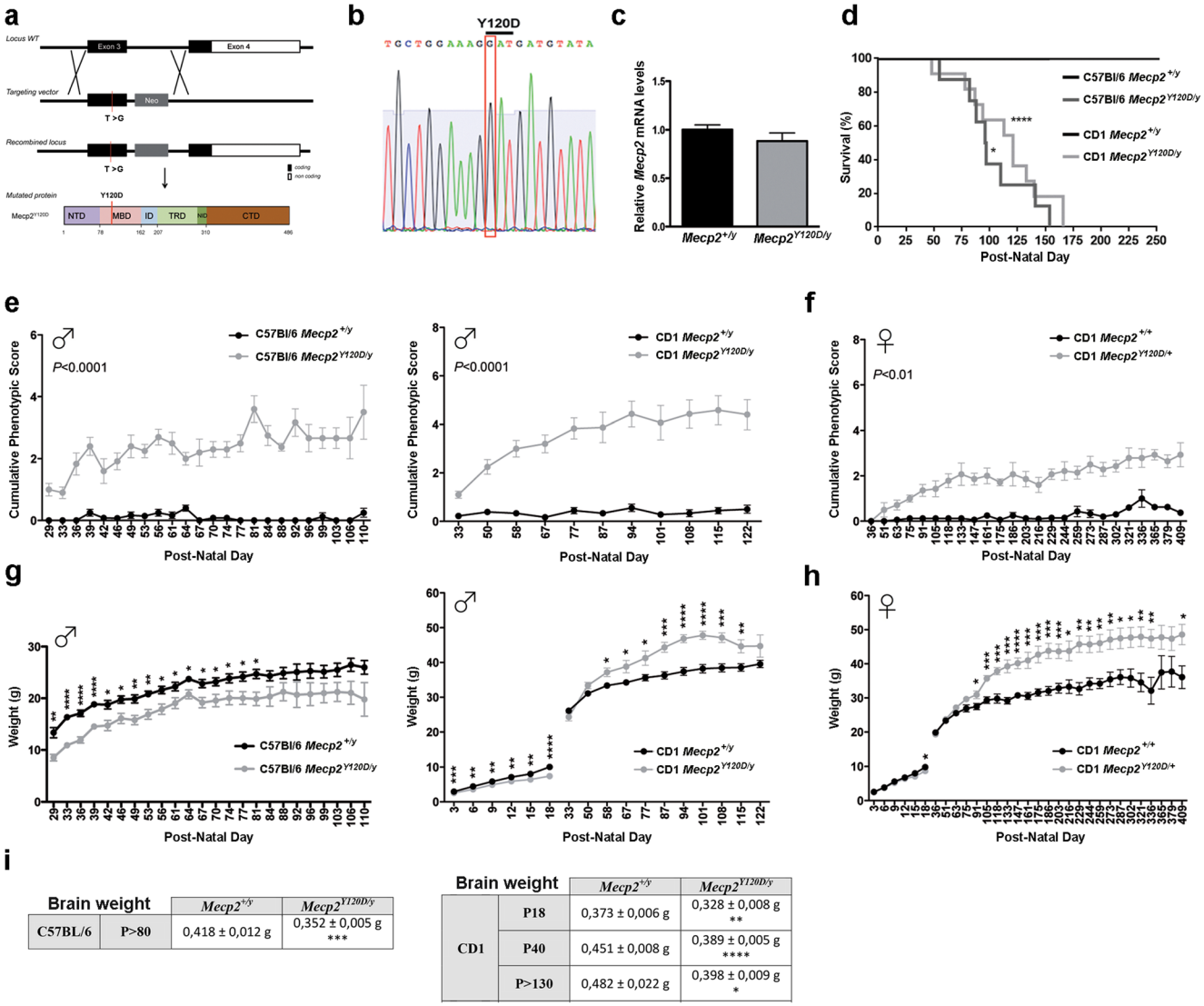

Fig. 1 The novel *Mecp2*^{Y120D} mouse line manifests severe RTT-like symptoms and short lifespan. **a** Schematic representation of the *Mecp2* locus targeting strategy exploited for the insertion of the Y120 mutation. See also Fig. S1. **b** DNA sequencing electropherogram showing the presence in the generated animals of the single point mutation T > G—highlighted—that leads to the substitution of Y120 with an aspartic acid (D). **c** qPCR assay shows no difference in the *Mecp2* mRNA levels of P30 C57BL/6J *Mecp2*$^{Y120D/y}$ ($n = 4$) cortices, compared to *Mecp2*$^{+/y}$ ($n = 3$). Data are represented relative to *Mecp2*$^{+/y}$, as mean ± s.e.m. Significance is calculated by Student's *t* test. **d** *Mecp2*$^{Y120D/y}$ mice in C57BL/6J and CD1 background ($n = 8$ and 11, respectively) show reduced lifespan compared to *Mecp2*$^{+/y}$ littermates ($n = 6$ and 9, respectively). Significance is calculated by Log-rank (Mantel-Cox) test (*$P < 0.05$, ****$P < 0.0001$). **e** Plots showing the progression of the phenotypic score (cumulated for general condition, mobility, hind limb clasping, and—only for CD1—tremor values) of C57BL/6J and CD1-mutated males (animals evaluated: $n = 6$ C57BL/6J and 10 CD1 *Mecp2*$^{Y120D/y}$ vs 7 C57BL/6J and 9 CD1 *Mecp2*$^{+/y}$). Analyses ended when there were less than three animals per group. Data are represented as mean ± s.e.m. Significance is calculated by two-way ANOVA. Plots of single variable are shown in Fig. S2. **f** Plot showing the progression of the phenotypic score (cumulated for general condition, mobility, hind limb clasping, and tremor values) of CD1 heterozygous females (animals evaluated: $n = 7$ *Mecp2*$^{Y120D/+}$ vs 8 *Mecp2*$^{+/+}$). Analyses ended when there were less than three animals per group. Data are represented as mean ± s.e.m. Significance is calculated by two-way ANOVA. Plots of single variable are shown in Fig. S2. **g** Plots showing the progression of total body weight of C57BL/6J and CD1-mutated males in comparison with control littermates (animals evaluated: C57BL/6J $n = 6$ *Mecp2*$^{Y120D/y}$ vs 7 *Mecp2*$^{+/y}$; CD1 pups $n = 19$ *Mecp2*$^{Y120D/y}$ vs $n = 17$ *Mecp2*$^{+/y}$; CD1 adult $n = 10$ *Mecp2*$^{Y120D/y}$ vs 9 *Mecp2*$^{+/y}$). Analyses ended when there were less than three animals per group. Data are represented as mean ± s.e.m. Significance is calculated by multiple *t* test (*$P < 0.05$, **$P < 0.01$, ***$P < 0.001$, ****$P < 0.0001$). **h** Plot showing the progression of total body weight of CD1 heterozygous females in comparison with control littermates (animals evaluated: pups $n = 18$ *Mecp2*$^{Y120D/+}$ vs $n = 14$ *Mecp2*$^{+/+}$; adult $n = 7$ *Mecp2*$^{Y120D/+}$ vs 8 *Mecp2*$^{+/+}$). Analyses ended when there were less than three animals per group. Data are represented as mean ± s.e.m. Significance is calculated by multiple *t* test (*$P < 0.05$, **$P < 0.01$, ***$P < 0.001$, ****$P < 0.0001$). **i** Brain weight was measured in juvenile (P18, $n = 4$ *Mecp2*$^{Y120D/y}$ vs 7 *Mecp2*$^{+/y}$), young adult (P40, $n = 18$ *Mecp2*$^{Y120D/y}$ vs 14 *Mecp2*$^{+/y}$), and adult (CD1 $P > 130$ $n = 4$ per genotype, C57BL/6J $P > 80$ $n = 5$ per genotype) mice. Measures of brain weights are expressed as mean ± s.e.m. Significance is calculated by Student's *t* test (*$P < 0.05$, **$P < 0.01$, ***$P < 0.001$, ****$P < 0.0001$)

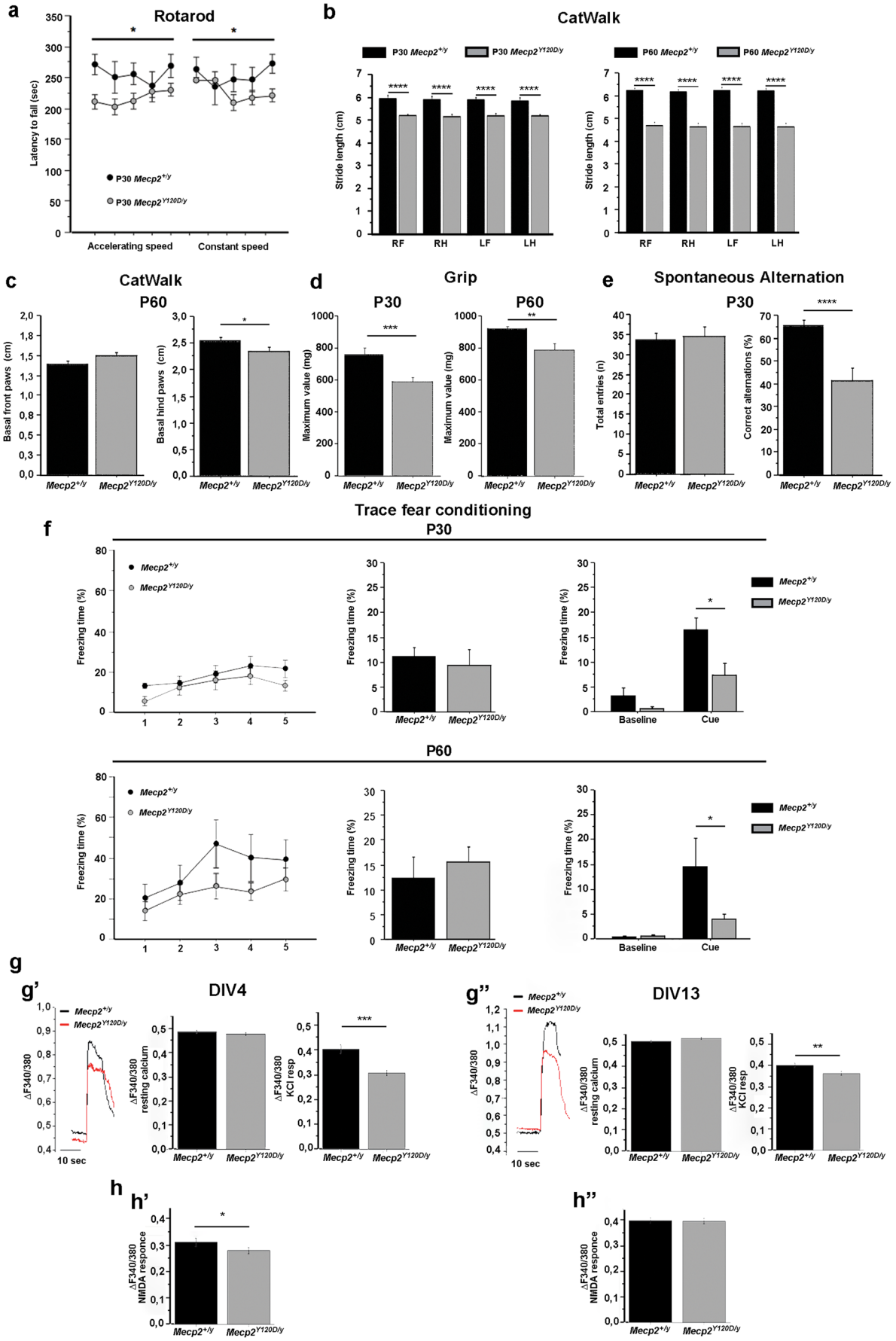
a
Rotarod
Latency to fall (sec)
P30 Mecp2+/y
P30 Mecp2Y120D/y
Accelerating speed
Constant speed
b
CatWalk
P30 Mecp2+/y
P30 Mecp2Y120D/y
P60 Mecp2+/y
P60 Mecp2Y120D/y
Stride length (cm)
RF
RH
LF
LH
c
CatWalk
P60
Basal front paws (cm)
Basal hind paws (cm)
Mecp2+/y
Mecp2Y120D/y
d
Grip
P30
P60
Maximum value (mg)
e
Spontaneous Alternation
P30
Total entries (n)
Correct alternations (%)
Trace fear conditioning
f
P30
P60
Freezing time (%)
Baseline
Cue
g
g'
DIV4
g''
DIV13
ΔF340/380
10 sec
ΔF340/380 resting calcium
ΔF340/380 KCl resp
h
h'
h''
ΔF340/380 NMDA responce

◀ **Fig. 2** CD1 *Mecp2*^{Y120D} mice are impaired in motor performance and short-term memory. See also Table S1. **a** Rotarod test showing the persistence on the rotating bar of P30 *Mecp2*$^{Y120D/y}$ ($n = 24$) compared to *Mecp2*$^{+/y}$ ($n = 14$) littermate mice. P30 *Mecp2*$^{Y120D/y}$ mice show altered motor coordination (acceleration phase, day 1) and increased muscle fatigue (constant speed, day 2). **b**, **c** Gait analyses with CatWalk XT software show small strides in the knock-in mice. Analyses were performed on P30 *Mecp2*$^{Y120D/y}$ ($n = 24$) and *Mecp2*$^{+/y}$ ($n = 14$), and P60 *Mecp2*$^{Y120D/y}$ ($n = 12$) and *Mecp2*$^{+/y}$ ($n = 16$) littermate mice. Stride length of right front (RF), right hind (RH), left front (LF), and left hind (LH) paws was measured in **b** and the base length of front and hind paws in **c**. **d** The strength of front paw muscles was measured through grip strength test on P30 *Mecp2*$^{Y120D/y}$ ($n = 24$) and *Mecp2*$^{+/y}$ ($n = 14$), and P60 *Mecp2*$^{Y120D/y}$ ($n = 12$) and *Mecp2*$^{+/y}$ ($n = 17$) littermate mice. The panel shows maximum values. **e** Working memory defects in P30 *Mecp2*$^{Y120D/y}$ ($n = 12$) and *Mecp2*$^{+/y}$ ($n = 17$) littermate mice assessed with the spontaneous alternation test. *Mecp2*$^{Y120D/y}$ mice show decreased percentage of correct alternation with the same number of entries compared to WT animals. **f** Impaired tone (cue; conditioned stimulus CS) memory in P30 *Mecp2*$^{Y120D/y}$ ($n = 13$) and P60 *Mecp2*$^{Y120D/y}$ ($n = 22$) mice compared to their *Mecp2*$^{+/y}$ littermates (P30, $n = 15$; P60, $n = 9$) during the auditory fear conditioning test. Graphs represent the percentage of freezing during the five tones (CS) of training phase (left panels), during the context test 24 h after training (middle panels) and during the cue test (right panels). Data are presented as means ± s.e.m. For statistical analyses, see "Materials and Methods" (*$P < 0.05$, **$P < 0.01$, ***$P < 0.001$, ****$P < 0.0001$). **g** Calcium imaging experiments in cultured E15.5 cortical neurons reveal precocious and persistent functional alterations in *Mecp2*$^{Y120D/y}$ neurons. Representative traces and relative quantification of KCl-induced calcium transients in WT and *Mecp2*$^{Y120D/y}$ cells are depicted. Whereas resting calcium levels are indistinguishable in the two groups during neuronal development (*Mecp2*$^{+/y}$ = 0.487 ± 0.005 vs *Mecp2*$^{Y120D/y}$ = 0.480 ± 0.006; *t* test Mann-Whitney rank sum test $P = 0.373$), KCl administration leads to reduced calcium influxes in both DIV4 (g' *Mecp2*$^{+/y}$ = 0.39 ± 0.013 vs *Mecp2*$^{Y120D/y}$ = 0.29 ± 0.009; *t* test Mann-Whitney rank sum test ***$P < 0.001$; number of analyzed cells *Mecp2*$^{+/y}$ = 184 vs *Mecp2*$^{Y120D/y}$ = 147) and DIV13 *Mecp2*$^{Y120D/y}$ cultures (g" *Mecp2*$^{+/y}$ = 0.404 ± 0.010 vs *Mecp2*$^{Y120D/y}$ = 0.368 ± 0.009; *t* test Mann-Whitney rank sum test **$P = 0.005$; number of analyzed cells *Mecp2*$^{+/y}$ = 155 vs *Mecp2*$^{Y120D/y}$ = 189; resting calcium levels *Mecp2*$^{+/y}$ = 0.50 ± 0.004 vs *Mecp2*$^{Y120D/y}$ = 0.52 ± 0.006; *t* test Mann-Whitney rank sum test $P = 0.096$). **h** NMDA delivery induces smaller calcium transients in immature DIV4-mutated neurons (h' DIV4; *Mecp2*$^{+/y}$ = 0.313 ± 0.011 vs *Mecp2*$^{Y120D/y}$ = 0.267 ± 0.011; *t* test *$P = 0.027$) and comparable calcium responses in mature cells (h" DIV13; *Mecp2*$^{+/y}$ = 0.409 ± 0.012 vs *Mecp2*$^{Y120D/y}$ = 0.408 ± 0.012; *t* test $p = 0.612$). Number of analyzed cells: *Mecp2*$^{+/y}$ DIV4 = 150, DIV13 = 184; *Mecp2*$^{Y120D/y}$ DIV4 = 150, DIV13 = 189)

the conditioned stimulus memory. By performing most of these tests also with CD1 *Mecp2*-null mice, we revealed that both *Mecp2* lines manifest very similar behavioral performances (Fig. S3).

Anxiety-like and explorative behaviors were also assayed through different approaches (Supplementary Materials and Table S1), but no significant defect was observed. Notably, while anxiety is a common trait of RTT patients, in *Mecp2* animal models, this feature depends on the specific genetic mutation [25].

We completed the preliminary assessment of phenotypes typically evaluated in *Mecp2* animal models by testing whether knock-in neurons exhibit functional defects similar to the *Mecp2*-null cells. We recently demonstrated that both in vivo and in vitro *Mecp2*-null neurons are characterized by a delayed maturation and impaired intrinsic responsiveness to external stimuli [26]. Thus, we cultured E15.5 *Mecp2*^{Y120D} cortical neurons and probed neuronal responsiveness; the analyses were performed on immature (DIV4) or more mature (DIV13) neurons (Fig. 2g). Calcium imaging analyses showed that the amplitude of KCl-induced calcium transients is reduced in mutated neurons both at DIV4 and 13, confirming an impairment in the expression/sensitivity of voltage-operated calcium channels (VOCCs) and consequently a defective neuronal responsiveness to depolarization. Calcium imaging was also used to obtain information on the expression of functional NMDA receptors (Fig. 2h). Whereas immature *Mecp2*^{Y120D} neurons showed a significant reduction in NMDA-induced calcium peaks, mature neurons exhibited normal calcium transients associated with NMDA stimulation in spite of lower response to KCl. These data confirm that *Mecp2* mutations affect neuronal responsiveness; further, they suggest that *Mecp2*-related phenotypes change along neuronal maturation.

Y120D Mutation Affects Mecp2 Abundance and Chromatin Binding Mainly in Mature Neurons

To gain insights into the molecular mechanisms responsible for the phenotypes affecting *Mecp2*^{Y120D} mice, we assessed Mecp2 levels and other molecular markers typically associated with Mecp2 functions. The results show that, while Mecp2-Y120D levels were normal in immature brains (E16, P6), they were significantly lower at P18 (− 56 ± 4%, ***$P < 0.001$, Student's t test; Fig. 3a) and P40 (− 62 ± 4%, ****$P < 0.0001$, Student's *t* test; Fig. 3a); a similar pattern was confirmed in in vitro cultured neurons (DIV7 − 29.7 ± 12.3%; DIV14 − 35.7 ± 13.3%, *$P < 0.05$, Student's *t* test; Fig. 3b).

In line with the *Mecp2*-null model, the mature knock-in brain (P40) exhibited a reduction in rpS6 phosphorylation (− 43 ± 4%, *$P < 0.05$, Student's *t* test; Fig. 3c, upper panel), a hallmark of RTT progression [27, 28]. Recently, we have demonstrated that phosphorylation of MeCP2 on Ser164 (S164), which is downregulated during neuronal maturation, globally diminishes MeCP2 binding to chromatin [19]. We thus assessed the levels of this phosphorylation in *Mecp2*$^{Y120D/y}$ adult mice, finding that it is significantly increased compared to WT (+ 193 ± 30%, ***$P < 0.001$, Student's *t* test; Fig. 3c, lower panel).

Since a 50% reduction of protein levels in mice cannot explain the severity of the observed phenotype [29], we proceeded analyzing the consequences of Y120D mutation on Mecp2 activity. Previous studies demonstrated that the MeCP2-Y120D mutant exogenously expressed in non-neuronal cells shows a reduced accumulation on heterochromatic foci [17, 18]. To confirm these results in cells expressing

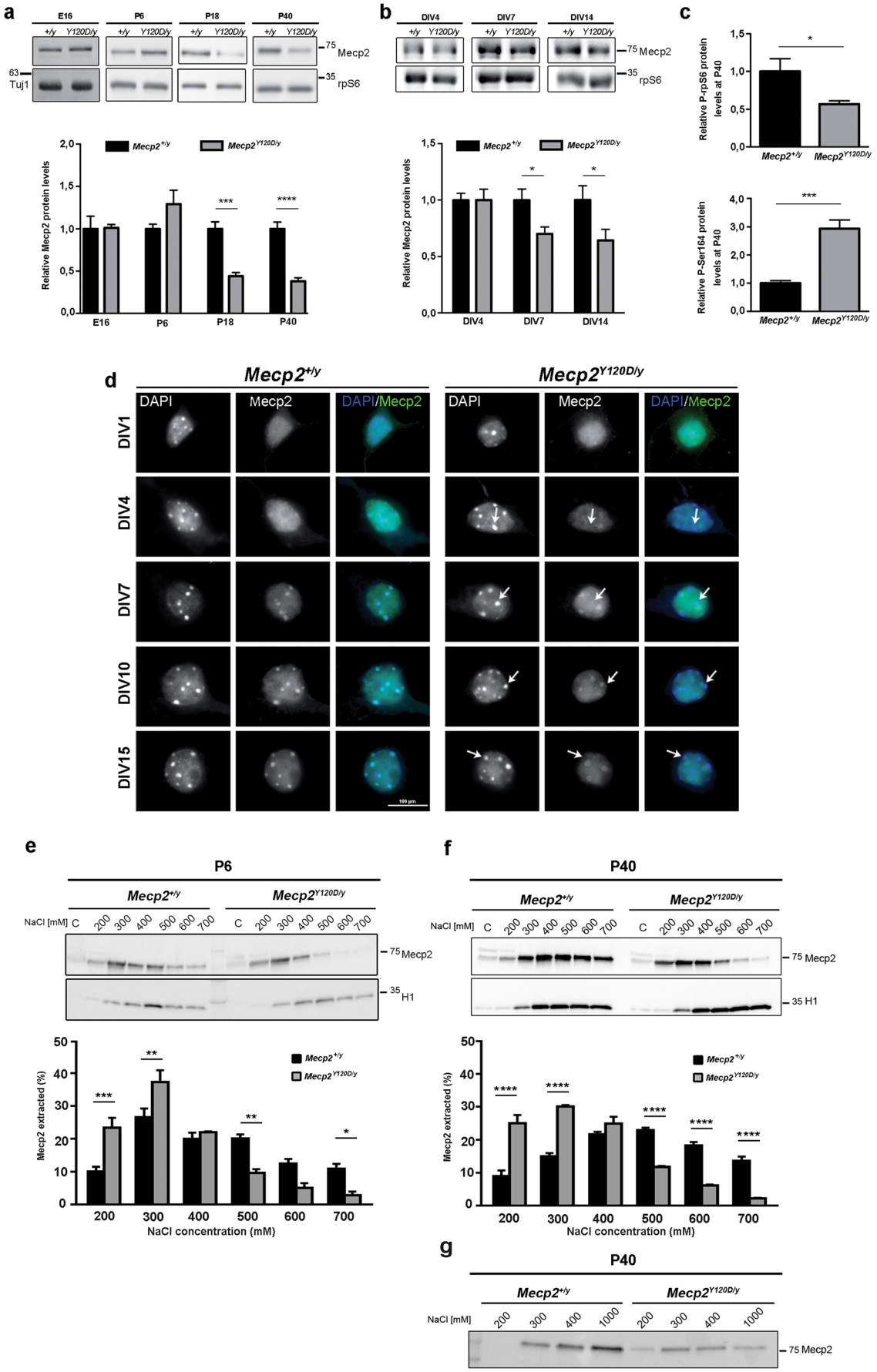
a
E16
P6
P18
P40
+/y
Y120D/y
63
Tuj1
75 Mecp2
35 rpS6
Relative Mecp2 protein levels
Mecp2+/y
Mecp2Y120D/y
b
DIV4
DIV7
DIV14
c
Relative P-rpS6 protein levels at P40
Relative P-Ser164 protein levels at P40
d
Mecp2+/y
Mecp2Y120D/y
DAPI
Mecp2
DAPI/Mecp2
DIV1
DIV4
DIV7
DIV10
DIV15
e
P6
NaCl [mM]
C
200
300
400
500
600
700
75 Mecp2
35 H1
Mecp2 extracted (%)
NaCl concentration (mM)
f
P40
g
1000

◀ **Fig. 3** The Y120D mutation affects Mecp2 abundance and its chromatin binding properties in mature neurons. **a** Representative images and western blot quantification of Mecp2 protein levels assessed on E16 brains and P6, P18, and P40 cortices of *Mecp2*$^{Y120D/y}$ and *Mecp2*$^{+/y}$ CD1 males ($n \geq 5$ per genotype at each time point). Data are represented relative to *Mecp2*$^{+/y}$, as mean ± s.e.m. Significance is calculated by Student's *t* test (***$P < 0.001$, ****$P < 0.0001$). **b** Representative images and western blot quantification of Mecp2 protein levels of *Mecp2*$^{Y120D/y}$ and *Mecp2*$^{+/y}$ E15.5 cortical neurons at different DIVs ($n \geq 10$ per genotype at each time point). Data are represented relative to *Mecp2*$^{+/y}$, as mean ± s.e.m. Significance is calculated by Student's *t* test (*$P < 0.5$). **c** Western blot quantification showing altered P-rpS6 and P-S164 levels in cortices of P40 *Mecp2*$^{Y120D/y}$ CD1 mice (n = 7 *Mecp2*$^{Y120D/y}$ vs 5 *Mecp2*$^{+/y}$). Data are represented relative to *Mecp2*$^{+/y}$, as mean ± s.e.m. Significance is calculated by Student's *t* test (*$P < 0.5$, ***$P < 0.001$). **d** Representative images of *Mecp2*$^{+/y}$ and *Mecp2*$^{Y120D/y}$ cultured neurons established from E17.5 cortices and immunostained at different DIV for DAPI (left panels) and Mecp2 (middle panels). *Mecp2*$^{Y120D/y}$ nuclei show diffused staining that does not overlap with DAPI-heterochromatic foci (white arrows). Images were taken at × 100 magnification. **e**, **f** Upper panels: representative western blots showing salt extraction of WT or mutant Mecp2 with increasing concentrations of NaCl from P6 and P40 mouse CD1 brains. H1 was included as control of the salt extraction procedure. Lower panels: quantification of the fraction of WT and Y120D Mecp2 extracted with different concentration of NaCl. Data are represented as mean ± s.e.m. Significance is calculated by two-way ANOVA followed by Bonferroni post hoc test (*$P < 0.05$, **$P < 0.01$, ***$P < 0.001$, ****$P < 0.0001$). **g** Nuclei were purified from *Mecp2*$^{+/y}$ and *Mecp2*$^{Y120D/y}$ P40 brains and resuspended in buffers containing 200 mM, 300 mM, 400 mM, or 1 M NaCl. Extracted Mecp2 was tested by western blot ($n = 2$)

physiological levels of Mecp2, we compared the sub-nuclear localization of the WT and mutated proteins in cultured cortical neurons (Fig. 3d). As expected, while the WT protein showed a clear accumulation on highly methylated heterochromatic foci starting from DIV7, Mecp2-Y120D remained mainly diffused in the nucleus along all stages of neuronal maturation, forming only few dots that do not overlap with DAPI-positive foci.

Our data thus suggest that the pathogenic mutation might directly and/or indirectly (through S164 phosphorylation [19]) impair Mecp2 affinity to chromatin, with the magnitude of the effect depending on brain maturation. Thus, through salt extraction experiments, we compared the affinity for chromatin of the WT and mutated protein in immature (P6) and mature (P40) mouse brains (Fig. 3e–g). As reported [19], in mature brain, WT Mecp2 is more tightly associated with chromatin compared to the immature brain. On the contrary, at P40, most of the mutant protein was extracted at 300 mM NaCl, therefore failing to acquire a tighter association with chromatin (Fig. 3f). To confirm this result with a complementary assay, an equal amount of brain nuclei isolated from WT and *Mecp2*^{Y120D} animals (P40) were incubated in buffers with increasing ionic strength and the amount of extracted Mecp2 analyzed by western blot (Fig. 3g). As already demonstrated [3], WT Mecp2 was increasingly extracted at higher salt concentrations; indeed, the highest signal was observed at 1 M NaCl, while almost no Mecp2 was detectable at 200 mM NaCl. On the contrary, most of Mecp2-Y120D was extracted with a much lower concentration of NaCl (300–400 mM) with no further increase at 1 M NaCl. Notably, the overall amount of the mutant protein was generally decreased in accordance with the protein levels depicted in Fig. 3a. Although the affinity for chromatin of WT and mutated Mecp2 diverged more clearly in mature brain, quantification of three independent experiments revealed that at P6, Mecp2-Y120D is already less tightly bound to chromatin (Fig. 3e).

Together, these data suggest that the Y120D mutation impairs both Mecp2 binding to chromatin and protein levels and that these phenotypes become progressively more evident when the WT MeCP2 acquires mature structural functions [7, 19].

Mecp2^{Y120D} and *Mecp2*-Null Brains Exhibit Different Chromatin Compaction

Mecp2 is known to interact with different chromatin remodeling complexes, and it is considered to play a major role in neuronal chromatin architecture [4, 30]. We thus addressed whether Mecp2-Y120D maintains its ability to interact with relevant corepressors, such as NCoR and ATRX and whether this mutation affects chromatin compaction.

Mecp2-null MEFs were cotransfected with eGFP or eGFP-MeCP2 derivatives and TBL1-mCherry, and the ability of MeCP2 isoforms to recruit TBL1, part of the NCoR complex, on heterochromatin foci was assessed. In accordance with [5, 31], we demonstrated that no cell transfected with eGFP showed co-localization of TBL1-mCherry with heterochromatic foci (Fig. 4a), whereas TBL1 was efficiently recruited on the DAPI-positive heterochromatic foci in 58% of cells expressing eGFP-MeCP2-WT and in 45% of cells expressing eGFP-MeCP2-Y120F. Importantly, only in 19% of cells expressing MeCP2-Y120D, TBL1-mCherry colocalized with the heterochromatic foci, suggesting that the interaction between Mecp2 and NCoR is significantly affected by the Y120D mutation. Of relevance, the presence of smaller and less bright green foci in cells that exogenously express eGFP-MeCP2-Y120D compared to cells transfected with eGFP-MeCP2-WT and eGFP-MeCP2-Y120F confirmed the impaired chromatin binding ability of the Y120D mutant.

Considering that the localization of the chromatin remodeling protein ATRX on pericentric heterochromatin of mouse neurons depends on its interaction with the MBD of Mecp2 [3, 6], we proceeded investigating and revealing a drastic change in ATRX localization in the *Mecp2*^{Y120D} brain with respect to controls (Fig. 4b). Together, these data confirm that the missense mutation Y120D alters the ability of MeCP2 to interact with and/or properly recruit on chromatin its corepressors, therefore affecting their sub-nuclear distribution. Given that such corepressors concur to chromatin landscaping, a

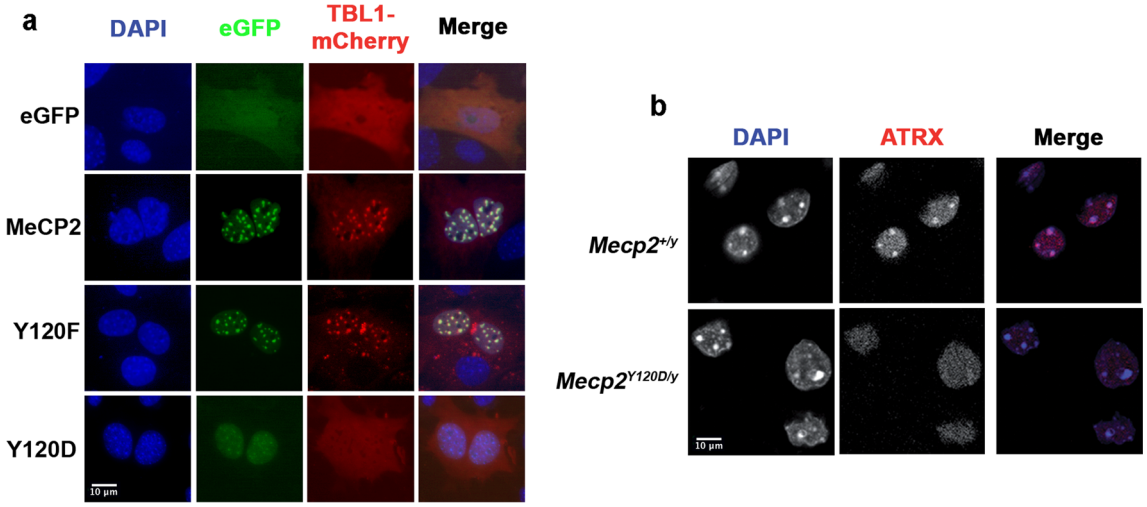

Fig. 4 The Y120D mutation affects the capacity of Mecp2 to recruit its corepressors on chromatin. **a** Representative images of *Mecp2*-null mouse embryonic fibroblasts (MEF) transfected with eGFP-MeCP2 derivatives to study the recruitment of the TBL1-mCherry construct on heterochromatic foci [5]. TBL1 is efficiently recruited on the DAPI-positive heterochromatic foci in 58% of cells expressing eGFP-MeCP2-WT ($n = 60$), in 45% of cells expressing eGFP-MeCP2-Y120F ($n = 60$) and only in 19% of the eGFP-MeCP2-Y120D ones ($n = 62$). In no cell transfected with eGFP alone, TBL1-mCherry ($n = 20$) was recruited on heterochromatic foci. Images were taken at × 40 magnification. The contrast and brightness parameters for each channel were adjusted to obtain a clear representation of the results. **b** Representative images showing the heterochromatic localization of ATRX in WT brains, in contrast to the diffuse staining of ATRX observable in Y120D sections ($n = 3$ animals per genotype; × 60 magnification)

time course of micrococcal nuclease (MNase) digestion of P6 and P40 brain nuclei was performed to analyze chromatin accessibility (Figs. 5a and S4). Interestingly, while we were unable to detect any overt phenotype in the immature brain (Fig. S4), the MNase digestion pattern at P40 of the *Mecp2*$^{Y120D/y}$ sample showed a slightly faster accumulation of fragments corresponding to mononucleosomal DNA normalized on total DNA (Fig. 5a). Quantification of three different experiments demonstrated a consistent trend that, however, did not reach the statistical significance (Fig. 5b'). By digesting WT and *Mecp2*-null chromatin, the mutant sample appeared mildly less accessible; this tendency was confirmed by quantifying three independent experiments (Fig. 5b"). Since these results might suggest that the complete absence of Mecp2 leads to compensatory mechanisms that differ from those generated by the presence of the mutated Mecp2, we corroborated these data with a complementary approach. Neuronal nuclei were thus purified from *Mecp2*$^{Y120D/y}$ or *Mecp2*-null adult (P40) cortices and the corresponding WT control tissues, and heterochromatic and euchromatic accessibility was assessed by staining purified nuclei with DAPI at different time points of MNase digestion. By measuring both the stained area in heterochromatic foci (Fig. 5c', left panel) and the average DAPI intensity (Fig. 5c", left panel) in Y120D samples, we revealed that euchromatic and heterochromatic DNA is more rapidly digested in mutant nuclei, therefore suggesting a globally more accessible chromatin structure. Conversely, MNase treatment of *Mecp2*-null nuclei demonstrated that their heterochromatic DNA, but not bulk chromatin, is less digested than the control (Fig. 5c', c", right panels). To verify whether this change in chromatin accessibility results in any functional alteration, transcriptional activity within single cortical nuclei was investigated by measuring the levels of phosphorylated RNA polymerase II (Pol II–S5P) in *Mecp2*$^{Y120D/y}$ or null P40 nuclei and their corresponding WT controls (Fig. 5d [32–35]). Signal specificity was confirmed by the lack of co-localization between DAPI foci (transcriptionally silent heterochromatin) and Pol II-S5P signal (transcriptionally active chromatin, Fig. 5d). Importantly, a strong and significant increase of Pol II-S5P in *Mecp2*$^{Y120D/y}$ nuclei was observed ($+53.4 \pm 1.3\%$, $^{****}P < 0.0001$, Student's *t* test; Fig. 5d'), while the null nuclei showed a slight but significant reduction with respect to their controls ($-22.9 \pm 0.9\%$, $^{****}P < 0.0001$, Student's *t* test; Fig. 5d").

Eventually, we reinforced these data analyzing whether WT, *Mecp2*-null, and *Mecp2*$^{Y120D/y}$ mature brain cortices (P40) differ in their 5-hydromethylcytosine (5-hmC) content. In fact, a direct relationship between genome accessibility, transcriptional activity, and 5-hmC levels has recently been proposed [36, 37]. In particular, methylated CG dinucleotides contained in highly compact chromatin are less frequently converted to 5-hmC, probably because of lower accessibility of Tet hydroxylases [36]. Figure 5e demonstrates that while *Mecp2*$^{Y120D/y}$ cortices manifest a tendency to an increase in 5-hmC levels, *Mecp2*-null adult brains display a small but significant decrement, as already reported for *Mecp2*-deficient granule cells [38].

Overall, these data support our hypothesis that the presence of Mecp2-Y120D diversely affects the general features of brain chromatin compared to the total absence of *Mecp2*.

Discussion

The generation of several mouse models carrying different *Mecp2* alterations proved instrumental to investigate MeCP2 functions and its involvement in Rett syndrome and *MECP2*-related disorders [10, 13]. *Mecp2*-null animals [8, 9] were the first model generated and still represent the mostly used one. However, it has recently become evident that when Mecp2 is absent, its functions are replaced by compensatory mechanisms that might mask and confound the consequences of its loss [7]. These results highlighted the importance of producing other models with less severe genetic lesions, possibly mimicking human mutations [5, 10, 12–14]. Our manuscript describes the generation and the behavioral and molecular characterization of a novel knock-in mouse model of Rett syndrome carrying the human missense mutation *MECP2-Y120D*, resulting in the substitution of tyrosine 120 (Y) with an aspartic acid (D) [16]. Although the Y120 residue of MeCP2 has been linked to RTT only once so far, its involvement in MeCP2 affinity for heterochromatin has already been proved [17, 18]. Through molecular dynamic simulations, we have recently demonstrated that the Y120D mutation leads the methyl binding domain (MBD) of MeCP2 to sample an alternative conformational space that impairs its ability to interact with DNA. These results have been experimentally confirmed in electrophoretic mobility shift assays comparing the ability of WT and Y120D MBD polypeptides to bind methylated and unmethylated DNA [15]. Interestingly, the conversion of Y120 into F did not affect the DNA binding properties of the MBD of MeCP2. Similarly, here, we demonstrate that WT and Y120F MeCP2 show a similar ability to recruit TBL1 on heterochromatin, while the mutant Y120D protein has lost such ability. All in all, these data suggest that harboring a tyrosine residue is not crucial for MeCP2 functions, while its conversion into aspartate, or possibly in a negatively charged residue, is a key detrimental step.

In line with the clinical features of the Y120D RTT patient [16], the Y120D mutation in mice leads to a harsh condition that is only slightly less severe compared to the total absence of the protein. Indeed, a progressive deterioration of the animal condition, in particular of the neurological aspects (mainly related to mobility, learning, and memory functions), becomes overt after a short period of apparently normal development, and eventually, these mice die prematurely.

The molecular characterization of this novel mouse model revealed several features that are highly relevant for research on MeCP2 and Rett syndrome.

First, although the Y120D mutation is supposed to impair Mecp2 binding to DNA, the molecular phenotypes associated with the mutant protein (reduced affinity for chromatin, inability to accumulate on heterochromatic foci, and bulk increase in chromatin accessibility) become evident mainly in mature neurons when protein levels are also halved. We recently suggested that Mecp2 changes its functions during brain maturation [19]. In particular, in developing brains and neurons, the protein is not tightly bound to chromatin and largely cosediments with nucleosome-free DNA. Possibly due to diverse post-translational modifications (i.e., phosphorylation) during brain maturation, MeCP2 attains a tight association with nucleosomal DNA and chromatin, probably also acquiring structural functions, as already proposed [7]. Thus, it is conceivable that the molecular consequences of harboring the missense mutation Y120D become more severe in adult brain, when mutant MeCP2 fails in acquiring its expected structural functions. Nevertheless, the impaired DNA binding is expected to somehow affect the transcriptional properties of MeCP2 also in early development, therefore leading to functional alterations. Accordingly, we demonstrate that early responsiveness to stimuli of $Mecp2^{Y120D}$ cultured neurons is impaired.

Theoretically, all MeCP2 mutants characterized by a reduced DNA binding should share the herein described molecular phenotypes. Indeed, an effect on protein stability of the RTT mutations T158M and R133C has already been proved. Interestingly, destabilization of mutant Mecp2 appeared to positively correlate with the reduction in DNA binding [12, 14]. However, in apparent discordance with our results, the $Mecp2^{T158A}$ mouse shows a significant decrement in protein levels already at perinatal age that worsens with time [14]. Similarly, Lamonica et al. found that the protein expression levels of the mutant $Mecp2^{T158M}$ are reduced of almost 20% at P0 and further decreased at P7 and P15; no further decrement was observed beyond this developmental stage [39].

So far, it is not clear why mutations in T158 cause an earlier effect on protein levels compared to Y120D. We propose that unbound Mecp2 is more rapidly degraded in mature neurons than in immature cells, which are physiologically characterized by a more dynamic association of the protein with chromatin. In addition, as already suggested [40], Mecp2 degradation might be affected by its post-translational modifications and it is conceivable that Mecp2-Y120D is diversely modified with respect to T158A/M. Accordingly, we demonstrate that the $Mecp2^{Y120D/y}$ mature brain exhibits a significant increase in S164 phosphorylation. However, since the Y120D mutation somehow mimics the effect of Y120 phosphorylation that occurs more frequently in the immature brain [15], it is also possible that the Y120D missense mutation has a minor impact on the developing brain compared to the T158M/A mutations. Thus, although in the future, we will investigate whether a different combination of post-translational modifications occurs on Mecp2-Y120D, currently, we cannot exclude that the mutated Mecp2 T158M protein is more impaired in its DNA binding properties and therefore more effectively degraded in the brain since early development.

Several studies suggest that one of the most relevant activities of MeCP2 in brain is the recruitment of corepressors on methylated DNA, leading to an inaccessible and

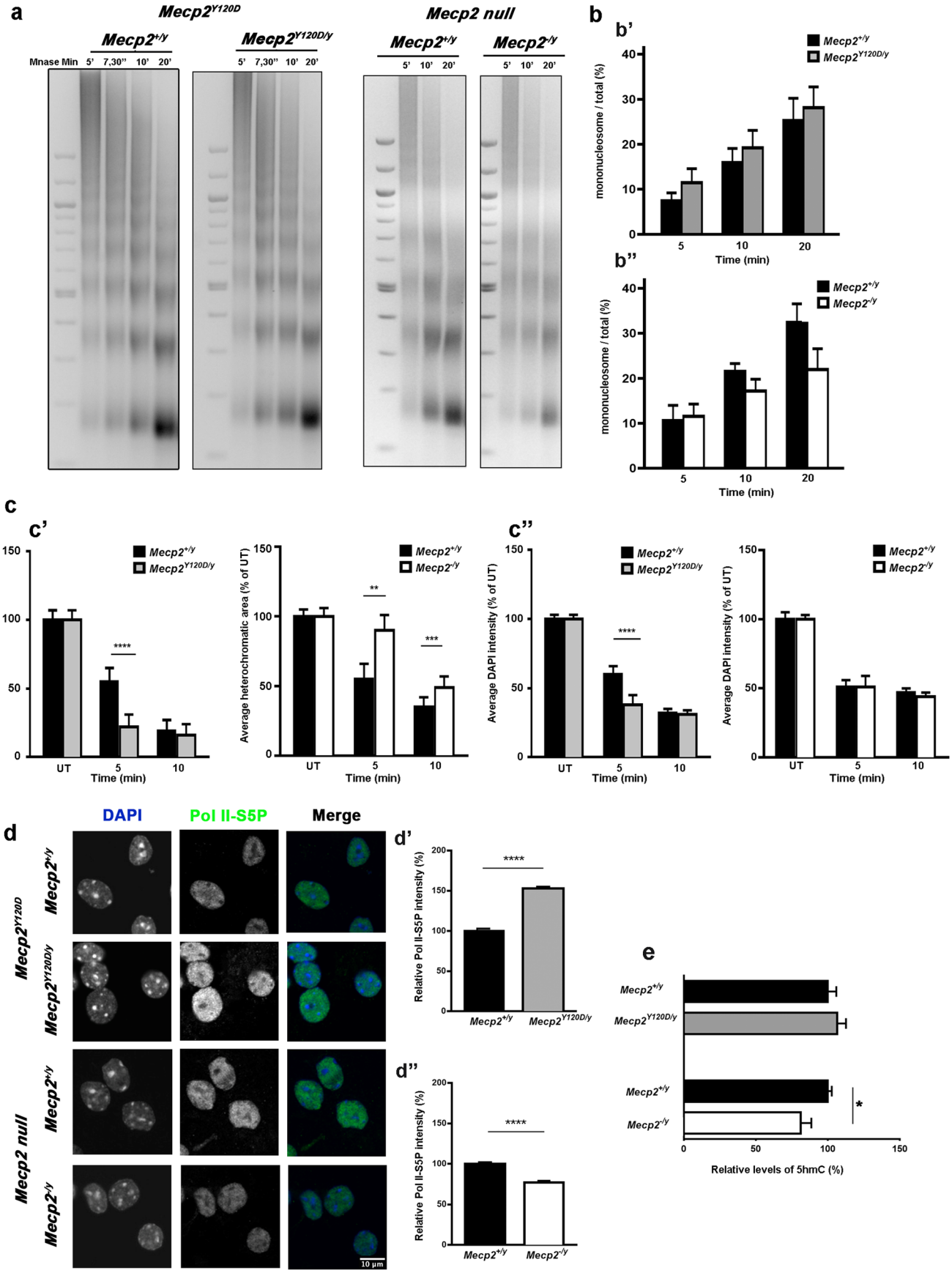
a
Mecp2Y120D
Mecp2+/y
Mecp2Y120D/y
Mecp2 null
Mecp2+/y
Mecp2-/y
Mnase Min 5' 7,30" 10' 20'
5' 7,30" 10' 20'
5' 10' 20'
5' 10' 20'
b
b'
Mecp2+/y
Mecp2Y120D/y
mononucleosome / total (%)
Time (min)
b"
Mecp2+/y
Mecp2-/y
mononucleosome / total (%)
Time (min)
c
c'
Mecp2+/y
Mecp2Y120D/y
Average heterochromatic area (% of UT)
UT
Time (min)
Mecp2+/y
Mecp2-/y
Average heterochromatic area (% of UT)
UT
Time (min)
c"
Mecp2+/y
Mecp2Y120D/y
Average DAPI intensity (% of UT)
UT
Time (min)
Mecp2+/y
Mecp2-/y
Average DAPI intensity (% of UT)
UT
Time (min)
d
DAPI
Pol II-S5P
Merge
Mecp2Y120D
Mecp2+/y
Mecp2Y120D/y
Mecp2 null
Mecp2+/y
Mecp2-/y
10 µm
d'
Relative Pol II-S5P intensity (%)
Mecp2+/y
Mecp2Y120D/y
d"
Relative Pol II-S5P intensity (%)
Mecp2+/y
Mecp2-/y
e
Mecp2+/y
Mecp2Y120D/y
Mecp2+/y
Mecp2-/y
Relative levels of 5hmC (%)

◀ **Fig. 5** *Mecp2*^{Y120D} brain exhibits different chromatin features compared to *Mecp2*-null and WT brains. **a** Representative images of chromatin accessibility assessed by digesting with MNase P40 *Mecp2*$^{+/y}$ and *Mecp2*$^{Y120D/y}$ and *Mecp2*$^{+/y}$ and *Mecp2*$^{-/y}$ brain nuclei. Purified digested DNA was loaded on a 2% agarose gel. For a similar analysis performed at P6, see Fig. S4. **b** Graphs showing the fraction of mononucleosomal DNA on total DNA at each time point (5, 10, and 20 min) of *Mecp2*$^{+/y}$ and *Mecp2*$^{Y120D/y}$ (b', $n = 3$) and *Mecp2*$^{+/y}$ and *Mecp2*$^{-/y}$ (b", $n = 3$) samples. Data are expressed as mean ± s.e.m. No statistical significance was reached by two-way ANOVA followed by Bonferroni post hoc test. **c** DAPI staining of MNase-treated nuclei isolated from P40 *Mecp2*$^{+/y}$ and *Mecp2*$^{Y120D/y}$ and *Mecp2*$^{+/y}$ and *Mecp2*$^{-/y}$ littermate cortices. Purified nuclei were digested with MNase for 5 and 10 min before staining. Undigested nuclei (UT) were DAPI stained for comparison ($n = 60$ to 110 nuclei for each experimental group). Heterochromatic area stained by DAPI was measured in *Mecp2*$^{Y120D/y}$ nuclei and *Mecp2*-null nuclei (c'), while total nuclear intensity is displayed in c". Data are expressed as percentage of the untreated WT and are represented as mean ± s.e.m. Significance was calculated by two-way ANOVA followed by Bonferroni post hoc test (**$P < 0.01$, ***$P < 0.001$, ****$P < 0.0001$). **d** *Mecp2*$^{Y120D/y}$ nuclei show higher Pol II-S5P transcriptional signal compared to *Mecp2*$^{-/y}$. Representative images of RNA Pol II S5P staining of *Mecp2*$^{Y120D/y}$ and *Mecp2*$^{-/y}$ cortical nuclei at P40 and their respective controls are displayed. Graphs represent the intensity of Pol II-S5P signal of d' *Mecp2*$^{+/y}$ and *Mecp2*$^{Y120D/y}$ nuclei and d" *Mecp2*$^{+/y}$ and *Mecp2*$^{-/y}$ nuclei ($n = 100$ nuclei for each experimental group). Data are expressed as percentage of WT and are represented as mean ± s.e.m. Significance is calculated by Student's *t* test (****$P < 0.0001$). **e** Graphs represent the percentage of 5-hmC in brain cortices of P40 *Mecp2*$^{+/y}$, *Mecp2*$^{Y120D/y}$, and *Mecp2*$^{-/y}$ mice ($n = 5$ for *Mecp2*$^{Y120D/y}$ and respective controls; $n = 5$ for *Mecp2*$^{-/y}$ and respective controls). Data are expressed as percentage of WT and are represented as mean ± s.e.m. Significance is calculated by Student's *t* test (*$P < 0.5$)

transcriptionally silent chromatin structure [4, 30]. Considering that in mature neurons, the protein is so abundant to bind the majority of methylated cytosines, its effects are likely exerted on the whole genome (Fig. 6, "WT"). We demonstrate that in cells expressing the Y120D mutant, the molecular partners of Mecp2, such as NCoR and ATRX, are not properly recruited on heterochromatin. As a result, in the *Mecp2*^{Y120D} mature brain, chromatin is globally more accessible compared to WT brain, in line with the increased levels of S5 phosphorylated RNA Polymerase II and the concomitant increase in 5-hmC levels, suggesting an increased transcriptional activity (Fig. 6, "Y120D"). Unexpectedly, the consequences of the total absence of Mecp2 are quite different and do not appear to cause the hypothesized general decrease in chromatin compaction [19]. Indeed, we found that mature *Mecp2*-null brains do not have a more accessible chromatin structure, but instead exhibit a reduced MNase accessibility particularly on heterochromatic DNA. Furthermore, *Mecp2*-null brain nuclei manifest reduced levels of actively transcribing RNA polymerase II and 5-hmC. Skene et al. proposed that in mature neurons, MeCP2 acts as a chromatin architectural factor whose absence is compensated by the up-regulation of histone H1 [7] (Fig. 6, "null"). Our data not only confirm the existence of compensatory mechanism(s) but also suggest that these compensations lead to a more packed chromatin structure. In possible accordance, several studies profiling transcription in *Mecp2*-null brains unexpectedly reported the down-regulation of the majority of differentially expressed genes [4, 27]; further, it has been suggested that histone H1 stabilizes a tighter chromatin structure compared to MeCP2 [41].

These data highlight that although mutations of *Mecp2* might produce largely concordant behavioral phenotypes in mice, they can diversely compromise Mecp2 functions, therefore leading to discordant compensatory mechanisms and/or alterations in chromatin structure. Although future studies will reveal the extent to which these diversities affect transcriptional profiles, our results indicate that effective therapeutic strategies might differ depending on the specific genetic mutation. For example, by increasing the expression of Mecp2-T158M, Lamonica et al. demonstrated that the reduced levels of the mutant protein are contributing to RTT pathogenesis [39]. Considering that mutations in the MBD might generally destabilize MeCP2, the authors proposed that therapies able to stabilize or increase the expression of mutant MeCP2 might have the potential to benefit most RTT patients carrying

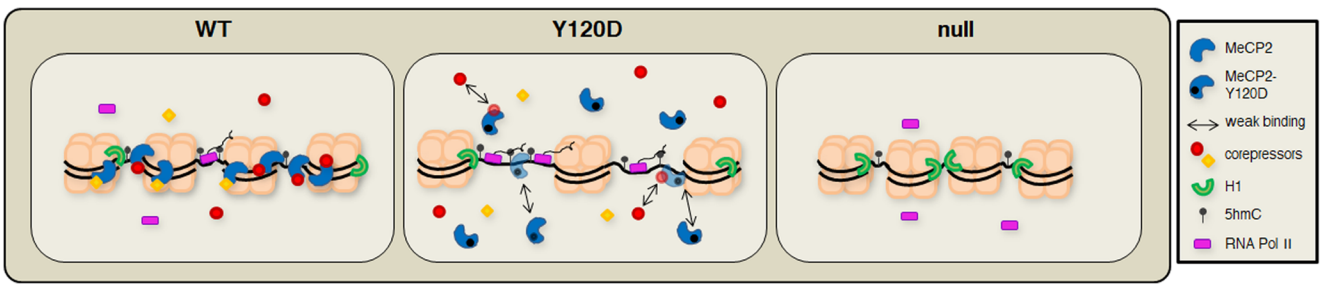

Fig. 6 A model for the different chromatin structure in *Mecp2*-null and *Mecp2*$^{Y120D/y}$ brains. Several studies have proposed that in brain MeCP2 is globally bound to chromatin where it recruits different remodeling chromatin complexes, therefore leading to a specialized chromatin structure ("WT" panel). Loss of MeCP2 protein would lead to compensatory mechanisms that double histone H1 levels [7] and lead to a more condensed and transcriptionally inert chromatin structure ("null" panel). In the Y120D knock-in brain, the labile interaction between MeCP2 and DNA, and the concomitant delocalization of its corepressors such as NCoR and ATRX lead to a more accessible and transcriptionally active chromatin structure ("Y120D" panel)

mutation in the MBD of MeCP2. However, we propose that the stabilization therapy might not be so beneficial in patients carrying a mutation that impairs the fundamental interaction of MeCP2 with NCoR [42], as it occurs with the MeCP2-Y120D alteration.

The molecular mechanism by which Y120D mutation impairs the NCoR binding is possibly due to a general change in the motions/dynamical profile of the MBD, while the T158M mutation mainly affects the structure of the domain [14]. Indeed, we demonstrated that, despite Y120 is not in direct contact with DNA, its mutation in D leads to an altered mobility of the domain and to a defective communication between the domain residues [15]. This impaired communication and profile of mobility/flexibility can be propagated to the entire protein, thus affecting the interaction with NCoR/SMRT. This long-range communication between the two protein domains could explain why the T158M and Y120D mutations have a different effect on the protein function although they are both located in the MBD.

To conclude, we suggest that only a thorough comprehension of the molecular alterations that affect *Mecp2*-null and knock-in animal lines mimicking human pathogenic mutations will truly highlight the molecular consequences of MeCP2 deficiency and the possible existence of convergent molecular defects. Emphasis should be given on comparing *Mecp2*-null models with animals carrying human mutations that affect or not affect MeCP2 binding to DNA together (or not) with an influence on its ability to associate with its interactors. These comparisons will help clarify whether treatment of *MECP2*-related diseases should consider a personalized approach in which patients are stratified in subgroups based on the molecular consequences of their genetic lesion.

Acknowledgments We are extremely grateful to Giovanni Tonon and Simona Segalla (San Raffaele Scientific Institute) for their helpful technical suggestions. Part of this work was carried out in ALEMBIC, an advanced microscopy laboratory established by IRCCS Ospedale San Raffaele and Università Vita-Salute San Raffaele.

Author Contributions A.G and N. L conceptualized and designed most of the study. P.D-A and F.A. assisted the design and realization of the behavioral and electrophysiological studies, respectively. A.G., E.B., A.B., B.L., C.C., S.C., G.S., L.P., V.B., F.B., M.P., and M.C. conducted the experiments, prepared most of the figures, and revised the manuscript. A.F. helped with statistical analysis of data. N.L. wrote the manuscript with the assistance of A.F. D.D-M, I.D., and C.K-N assisted in interpreting and discussing results.

Funding Information This work was mainly supported by the Italian parents' association "pro RETT ricerca" to N.L. Financial support was from Fondazione Telethon, Italy (Grant no. GGP16015 to F.A.). Functional experiments were supported by the Italian Ministry of Research and Education program "FIRB giovani" 2010, protocol number RBFR10ZBYZ. Fondazione Veronesi (Milan, Italy) provided additional funding to F.B.

Compliance with Ethical Standards

Research involving animals was performed in accordance with the European Community Council Directive 2010/63/UE for care and use of experimental animals; all the protocols were approved by the Italian Minister for Scientific Research and by the San Raffaele Scientific Institutional Animal Care and Use Committee in accordance with the Italian law.

Conflict of Interest The authors declare that they have no conflict of interest.

References

1. Amir RE, Van den Veyver IB, Wan M et al (1999) Rett syndrome is caused by mutations in X-linked MECP2, encoding methyl-CpG-binding protein 2. Nat Genet 23:185–188. https://doi.org/10.1038/13810
2. Neul JL, Kaufmann WE, Glaze DG et al (2010) Rett syndrome: revised diagnostic criteria and nomenclature. Ann Neurol 68:944–950. https://doi.org/10.1002/ana.22124
3. Baker SA, Chen L, Wilkins AD, Yu P, Lichtarge O, Zoghbi HY (2013) An AT-hook domain in MeCP2 determines the clinical course of Rett syndrome and related disorders. Cell 152:984–996. https://doi.org/10.1016/j.cell.2013.01.038
4. Bedogni F, Rossi RL, Galli F, Cobolli Gigli C, Gandaglia A, Kilstrup-Nielsen C, Landsberger N (2014) Rett syndrome and the urge of novel approaches to study MeCP2 functions and mechanisms of action. Neurosci Biobehav Rev 46:187–201. https://doi.org/10.1016/j.neubiorev.2014.01.011
5. Lyst MJ, Ekiert R, Ebert DH, Merusi C, Nowak J, Selfridge J, Guy J, Kastan NR et al (2013) Rett syndrome mutations abolish the interaction of MeCP2 with the NCoR/SMRT co-repressor. Nat Neurosci 16:898–902. https://doi.org/10.1038/nn.3434
6. Nan X, Hou J, Maclean A, Nasir J, Lafuente MJ, Shu X, Kriaucionis S, Bird A (2007) Interaction between chromatin proteins MECP2 and ATRX is disrupted by mutations that cause inherited mental retardation. Proc Natl Acad Sci 104:2709–2714. https://doi.org/10.1073/pnas.0608056104
7. Skene PJ, Illingworth RS, Webb S, Kerr ARW, James KD, Turner DJ, Andrews R, Bird AP (2010) Neuronal MeCP2 is expressed at near histone-octamer levels and globally alters the chromatin state. Mol Cell 37:457–468. https://doi.org/10.1016/j.molcel.2010.01.030
8. Chen RZ, Akbarian S, Tudor M, Jaenisch R (2001) Deficiency of methyl-CpG binding protein-2 in CNS neurons results in a Rett-like phenotype in mice. Nat Genet 27:327–331. https://doi.org/10.1038/85906
9. Guy J, Hendrich B, Holmes M, Martin JE, Bird A (2001) A mouse Mecp2-null mutation causes neurological symptoms that mimic Rett syndrome. Nat Genet 27:322–326. https://doi.org/10.1038/85899
10. Ricceri L, De Filippis B, Laviola G (2008) Mouse models of Rett syndrome: from behavioural phenotyping to preclinical evaluation of new therapeutic approaches. Behav Pharmacol 19:501–517. https://doi.org/10.1097/FBP.0b013e32830c3645
11. Stearns NA, Schaevitz LR, Bowling H, Nag N, Berger UV, Berger-Sweeney J (2007) Behavioral and anatomical abnormalities in Mecp2 mutant mice: a model for Rett syndrome. Neuroscience 146:907–921. https://doi.org/10.1016/j.neuroscience.2007.02.009
12. Brown K, Selfridge J, Lagger S, Connelly J, de Sousa D, Kerr A, Webb S, Guy J et al (2016) The molecular basis of variable phenotypic severity among common missense mutations causing Rett

syndrome. Hum Mol Genet 25:558–570. https://doi.org/10.1093/hmg/ddv496

13. Bellini E, Pavesi G, Barbiero I, Bergo A, Chandola C, Nawaz MS, Rusconi L, Stefanelli G et al (2014) MeCP2 post-translational modifications: a mechanism to control its involvement in synaptic plasticity and homeostasis? Front Cell Neurosci 8:236. https://doi.org/10.3389/fncel.2014.00236
14. Goffin D, Allen M, Zhang L, Amorim M, Wang ITJ, Reyes ARS, Mercado-Berton A, Ong C et al (2012) Rett syndrome mutation MeCP2 T158A disrupts DNA binding, protein stability and ERP responses. Nat Neurosci 15:274–283. https://doi.org/10.1038/nn.2997
15. D'Annessa I, Gandaglia A, Brivio E et al (2018) Tyr120Asp mutation alters domain flexibility and dynamics of MeCP2 DNA binding domain leading to impaired DNA interaction: atomistic characterization of a Rett syndrome causing mutation. Biochim Biophys Acta Gen Subj 1862:1180–1189. https://doi.org/10.1016/j.bbagen.2018.02.005
16. Inui K, Akagi M, Ono J, Tsukamoto H, Shimono K, Mano T, Imai K, Yamada M et al (2001) Mutational analysis of MECP2 in Japanese patients with atypical Rett syndrome. Brain and Development 23:212–215. https://doi.org/10.1016/S0387-7604(01)00197-8
17. Agarwal N, Becker A, Jost KL, Haase S, Thakur BK, Brero A, Hardt T, Kudo S et al (2011) MeCP2 Rett mutations affect large scale chromatin organization. Hum Mol Genet 20:4187–4195. https://doi.org/10.1093/hmg/ddr346
18. Kudo S, Nomura Y, Segawa M, Fujita N, Nakao M, Schanen C, Tamura M (2003) Heterogeneity in residual function of MeCP2 carrying missense mutations in the methyl CpG binding domain. J Med Genet 40:487–493. https://doi.org/10.1136/jmg.40.7.487
19. Stefanelli G, Gandaglia A, Costa M, Cheema MS, di Marino D, Barbiero I, Kilstrup-Nielsen C, Ausió J et al (2016) Brain phosphorylation of MeCP2 at serine 164 is developmentally regulated and globally alters its chromatin association. Sci Rep 6:28295. https://doi.org/10.1038/srep28295
20. Bergo A, Strollo M, Gai M et al (2015) Methyl-CpG binding protein 2 (MeCP2) localizes at the centrosome and is required for proper mitotic spindle organization. J Biol Chem 290:3223–3237. https://doi.org/10.1074/jbc.M114.608125
21. Cobolli Gigli C, Scaramuzza L, Gandaglia A, Bellini E, Gabaglio M, Parolaro D, Kilstrup-Nielsen C, Landsberger N et al (2016) MeCP2 related studies benefit from the use of CD1 as genetic background. PLoS One 11:e0153473. https://doi.org/10.1371/journal.pone.0153473
22. Guy J, Gan J, Selfridge J, Cobb S, Bird A (2007) Reversal of neurological defects in a mouse model of Rett syndrome. Science 315:1143–1147. https://doi.org/10.1126/science.1138389
23. Antonucci F, Corradini I, Morini R, Fossati G, Menna E, Pozzi D, Pacioni S, Verderio C et al (2013) Reduced SNAP-25 alters short-term plasticity at developing glutamatergic synapses. EMBO Rep 14:645–651. https://doi.org/10.1038/embor.2013.75
24. Shahbazian MD, Young JI, Yuva-Paylor LA, Spencer CM, Antalffy BA, Noebels JL, Armstrong DL, Paylor R et al (2002) Mice with truncated MeCP2 recapitulate many Rett syndrome features and display hyperacetylation of histone H3. Neuron 35:243–254. https://doi.org/10.1016/S0896-6273(02)00768-7
25. Katz DM, Berger-Sweeney JE, Eubanks JH, Justice MJ, Neul JL, Pozzo-Miller L, Blue ME, Christian D et al (2012) Preclinical research in Rett syndrome: setting the foundation for translational success. Dis Model Mech 5:733–745. https://doi.org/10.1242/dmm.011007
26. Bedogni F, Cobolli Gigli C, Pozzi D, Rossi RL, Scaramuzza L, Rossetti G, Pagani M, Kilstrup-Nielsen C et al (2016) Defects during Mecp2 null embryonic cortex development precede the onset of overt neurological symptoms. Cereb Cortex 26:2517–2529. https://doi.org/10.1093/cercor/bhv078
27. Li Y, Wang H, Muffat J, Cheng AW, Orlando DA, Lovén J, Kwok SM, Feldman DA et al (2013) Global transcriptional and translational repression in human-embryonic-stem-cell-derived Rett syndrome neurons. Cell Stem Cell 13:446–458. https://doi.org/10.1016/j.stem.2013.09.001
28. Ricciardi S, Boggio EM, Grosso S, Lonetti G, Forlani G, Stefanelli G, Calcagno E, Morello N et al (2011) Reduced AKT/mTOR signaling and protein synthesis dysregulation in a Rett syndrome animal model. Hum Mol Genet 20:1182–1196. https://doi.org/10.1093/hmg/ddq563
29. Samaco RC, Fryer JD, Ren J, Fyffe S, Chao HT, Sun Y, Greer JJ, Zoghbi HY et al (2008) A partial loss of function allele of methyl-CpG-binding protein 2 predicts a human neurodevelopmental syndrome. Hum Mol Genet 17:1718–1727. https://doi.org/10.1093/hmg/ddn062
30. Guy J, Cheval H, Selfridge J, Bird A (2011) The role of MeCP2 in the brain. Annu Rev Cell Dev Biol 27:631–652. https://doi.org/10.1146/annurev-cellbio-092910-154121
31. Kruusvee V, Lyst MJ, Taylor C, Tarnauskaitė Ž, Bird AP, Cook AG (2017) Structure of the MeCP2–TBLR1 complex reveals a molecular basis for Rett syndrome and related disorders. Proc Natl Acad Sci 114:E3243–E3250. https://doi.org/10.1073/pnas.1700731114
32. Egloff S, Murphy S (2008) Role of the C-terminal domain of RNA polymerase II in expression of small nuclear RNA genes. Biochem Soc Trans 36:537–539. https://doi.org/10.1042/BST0360537
33. Hirose Y, Ohkuma Y (2007) Phosphorylation of the C-terminal domain of RNA polymerase II plays central roles in the integrated events of eucaryotic gene expression. J Biochem 141:601–608. https://doi.org/10.1093/jb/mvm090
34. Linhoff MW, Garg SK, Mandel G (2015) A high-resolution imaging approach to investigate chromatin architecture in complex tissues. Cell 163:246–255. https://doi.org/10.1016/j.cell.2015.09.002
35. Phatnani HP, Greenleaf AL (2006) Phosphorylation and functions of the RNA polymerase II CTD. Genes Dev 20:2922–2936. https://doi.org/10.1101/gad.1477006
36. Lister R, Mukamel EA, Nery JR, Urich M, Puddifoot CA, Johnson ND, Lucero J, Huang Y et al (2013) Global epigenomic reconfiguration during mammalian brain development. Science 1237905–1237905:341. https://doi.org/10.1126/science.1237905
37. Ludwig AK, Zhang P, Hastert FD, Meyer S, Rausch C, Herce HD, Müller U, Lehmkuhl A et al (2017) Binding of MBD proteins to DNA blocks Tet1 function thereby modulating transcriptional noise. Nucleic Acids Res 45:2438–2457. https://doi.org/10.1093/nar/gkw1197
38. Mellén M, Ayata P, Dewell S, Kriaucionis S, Heintz N (2012) MeCP2 binds to 5hmC enriched within active genes and accessible chromatin in the nervous system. Cell 151:1417–1430. https://doi.org/10.1016/j.cell.2012.11.022
39. Lamonica JM, Kwon DY, Goffin D, Fenik P, Johnson BS, Cui Y, Guo H, Veasey S et al (2017) Elevating expression of MeCP2 T158M rescues DNA binding and Rett syndrome–like phenotypes. J Clin Invest 127:1889–1904. https://doi.org/10.1172/JCI90967
40. Thambirajah AA, Eubanks JH, Ausió J (2009) MeCP2 post-translational regulation through PEST domains: two novel hypotheses. BioEssays 31:561–569. https://doi.org/10.1002/bies.200800220
41. Riedmann C, Fondufe-Mittendorf YN (2016) Comparative analysis of linker histone H1, MeCP2, and HMGD1 on nucleosome stability and target site accessibility. Sci Rep 6:33186. https://doi.org/10.1038/srep33186
42. Tillotson R, Selfridge J, Koerner MV, Gadalla KKE, Guy J, de Sousa D, Hector RD, Cobb SR et al (2017) Radically truncated MeCP2 rescues Rett syndrome-like neurological defects. Nature 550:398–401. https://doi.org/10.1038/nature24058